Journal of Materials Chemistry A

Accepted Manuscript

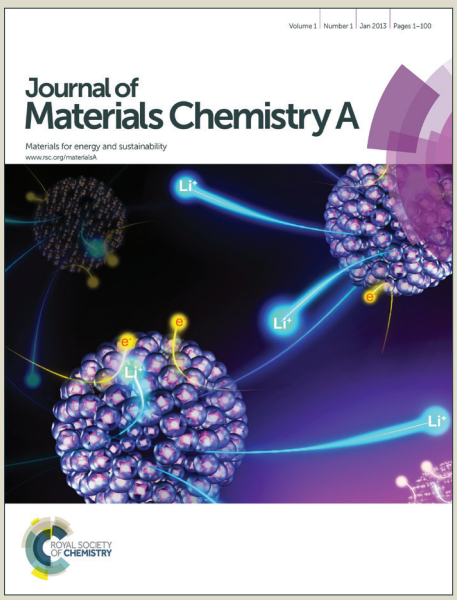

ROYAL SOCIETY OF CHEMISTRY

www.rsc.org/materialsA

Significantly enhanced thermoelectric figure of merit of p-type Mg_3Sb_2-based Zintl phase compound via nanostructuring employing high energy mechanical milling coupled with spark plasma sintering

A. Bhardwaj[1, 2] N.S. Chauhan[1, 2] and D. K. Misra[1,2]*

[1]CSIR-Network of Institutes for Solar Energy, Physics of Energy Harvesting, CSIR-National Physical Laboratory, Dr. K. S. Krishnan Marg, New Delhi-110012, India.

[2]Academy of Scientific & Innovative Research (AcSIR), CSIR-National Physical Laboratory (CSIR-NPL) campus, New Delhi-110012, India.

Abstract:

Several nanostructuring methods have been demonstrated to produce variants of nanostructured materials and these methods are well recognized as effective paradigms for improving the performance of thermoelectric materials. Among the variants of nanostructured materials, bulk nanostructured materials have been shown to be most promising materials due to not only high ZT but they can be fabricated in large quantities unlike to many other nanostructured materials making them desirable for large scale industrial application. In this paper, nanostructuring paradigm is extended for the first time to the bulk Mg_3Sb_2 and $Mg_3Sb_{1.8}Bi_{0.2}$ Zintl phase compounds which despite advantages of price and abundancy, so far has been disregarded for thermoelectric research, due to low ZT relative to the available state-of-the-art thermoelectric materials. Nanostructuring of bulk Mg_3Sb_2 and $Mg_3Sb_{1.8}Bi_{0.2}$ employing high energy ball milling and followed by spark plasma sintering yields a ZT~ 0.4 and a ZT~0.94 at 773 K respectively which are 54% and 56% higher values than their respective bulk counterparts. The enhancement in ZT of these materials is primarily due to the significant reduction in thermal conductivity

caused by phonon scattering at numerous grain boundaries of nanostructured materials. The observed decrease in thermal conductivity of these bulk nanostructured materials is quantified using a simple model that combines the macroscopic effective medium approaches (EMA) with the concepts of Kapitza resistance. The microstructure investigation of these nanostructured materials was carried out employing high resolution transmission electron microscopy (HRTEM).

*Corresponding author: E-mail: misradk@nplindia.org OR dakkmisra@gmail.com (DKM)

INTRODUCTION

Globally, outpacing production and consumption of energy and their direct and indirect environmental impacts has raised an urge to develop effective energy conversion technologies. Out of several energy conversion technologies, thermoelectric energy conversion of heat into electricity and vice-versa by using of materials so called as thermoelectric materials, is receiving tremendous amount of interest and attention.[1-3] Despite of their high reliability, simplicity and of course their unique technical merits, thermoelectricity could find only few niche applications mainly due to their low conversion efficiency.[4] The much wider applications of these materials require designing high performance thermoelectric materials. Thermoelectric material design primarily centers on optimizing its figure of merit defined as $ZT = S^2\sigma T/\kappa$ where S represents the Seebeck coefficient, σ the electrical conductivity, κ ($= \kappa_e + \kappa_l$) the thermal conductivity which includes contributions from the charge carriers (κ_e) and from the lattice (κ_l), and T the absolute temperature.[5] Therefore, to attain maximum thermoelectric performance, the power factor ($= S^2\sigma$) needs to be increased with simultaneous decrease in thermal conductivity (κ). However, the carrier density considerations inhibit any increase in S often leads to decrease in σ. Further, σ

and κ are also coupled through the Wiedemann-Franz law and thus an increase in σ simultaneously leads to increase in κ as well.[5]

The current strategies to improve the ZT are focused on circumventing the interdependencies of these three competing parameters by simultaneous optimization of the power factor and reduction in the thermal conductivity through several strategies such as doping,[6-9] solid solution alloying,[10-14] several ideally engineered materials[15-17] and materials developed based on the phonon glass and electron crystal (PGEC) concept,[18-20] and nanostructuring/nanocomposites.[21-25] Among all these strategies, nanostructuring approach has made a marked recognition in achieving high ZT of thermoelectric materials. This approach suggests that the ZT enhancement can be realized due to nanoscale size of grains or nanostructured morphologies of the materials.[26-28] The small grain sizes of these nanostructured materials leads to a drastic increase in the density of grain boundaries. The high concentration of grain boundaries is expected to lower the lattice thermal conductivity of the materials. As, nanostructuring introduces numerous interfaces in which phonons over a large mean free path range can be scattered more effectively and preferentially than electrons, thereby reducing the lattice thermal conductivity effectively while preserving carrier mobility and electronic conduction can be persisted. Moreover, the density of states (DOS) near Fermi level can also be enhanced in nanostructured materials via quantum confinement resulting to increase Seebeck coefficient. Despite to high density of grains in nanostructured material, the scattering of electrons in nanostructured samples do not take place effectively because of much shorter mean free path of electrons and thereby maintains the electrical conductivity together with high Seebeck coefficient contrary to the usual observation. Thus the nanostructuring can provide an efficient way to decouple all the three competing parameters; Seebeck coefficient, electrical conductivity and thermal conductivity up to a certain

extent.[26-28] However, Biswas et al.[29] established an endotaxial nanostructuring approach derived by precipitation and growth mechanism for even better optimization of electronic properties along with the significant reduction in thermal conductivity, resulting to high ZT.

Based on these unique features of nanostructured materials, variants of nanostructures in different dimensions such as superlattices,[30] quantum dots,[31] and nanowires[32,33] have also been designed with an appreciable improvement in their thermoelectric response. However, the high ZT in such artificially tailored nanostructured materials are not much of practical use in large-scale commercial applications because their nano-fabrication processes are rather tedious and hence expensive. On the other hand, a nanostructured material fabricated using a bulk process rather than nanofabrication techniques, has the advantage of being able to be produced in large quantities and in a form that is compatible with commercially available devices.[24-28,34-36]

In this present work, the premises of nanostructuring approach has been extended for the first time to a potential p-type bulk Zintl phase compound of Mg_3Sb_2[11-13,37-41] and also to its derivative $Mg_3Sb_{1.8}Bi_{0.2}$ studied previously by our group.[11] Mg_3Sb_2-based materials are an important class of thermoelectric materials belonging to Zintl phase family. These materials exhibit phonon glass and electron crystal (PGEC) behaviour rendering low thermal conductivity similar to that of glass and electrically conducting like metal and the same is requisite feature of a material to be a potential thermoelectric. Thus looking at the potentiality on thermoelectricity of these materials and using the premises of nanostructuring approach, high energy ball milling (HEBM) of bulk single phase of Mg_3Sb_2 and $Mg_3Sb_{1.8}Bi_{0.2}$ materials for different period of milling e.g. 10, 20 and 30 hrs have been performed to examine the nanostructuring effect on thermoelectric properties. The consolidation of these mechanically alloyed nanopowders was carried out employing spark plasma assisted (SPS) reaction sintering to synthesize the bulk

nanostructured materials in the form of dense pellets. The consolidation and sintering by SPS is well known technique to retard the grain growth. In SPS process, high energy current pulses are passed through the graphite die which contain the ball milled nano-powder under pressure, which momentarily generates a plasma between the grains resulting in highly localized temperatures.[42,43] The rapid heating rates combined with pressure result in achieving samples of near theoretical density. Unlike the hot-pressing technique, the extremely short sintering time cycle in SPS prohibits mass transport and hence the grain growth and thus retains nanostructured features achieved during ball-milling. [42,43] Further, the homogeneity in the sintered sample is an added advantage of SPS. Interestingly, bulk nanostructured materials were resulted after SPS which have been examined by HRTEM investigation. An enhanced ZT ~ 0.4 at 773K was observed for bulk nanostructured Mg_3Sb_2 which is ~ 54 % larger than its bulk counterpart (i.e. ZT~ 0.26 at 773K). Similarly, an enhanced ZT~0.94 at 773 K was observed in bulk nanostructured $Mg_3Sb_{1.8}Bi_{0.2}$ sample, which is comparable to other state-of-the-art thermoelectric materials. This enhancement in ZT is ~56% higher than its bulk counterpart (i.e. ZT~ 0.6 at 773K). The reduction in thermal conductivity of these materials resulted due to effective phonon scattering at numerous grain boundaries is attributed as a primary cause for high ZT. The effect of grain boundary scattering on the thermal conductivity is investigated in a framework of a simple model describing the macroscopic effective medium approaches with the concept of the Kapitza resistance proposed by Nan et al.[44-47]

2. Experimental section

2.1 Synthesis

Stoichiometric amounts of high purity elements magnesium (Mg; 99.99%, Alfa Aesar), antimony (Sb; 99.99%, Alfa Aesar), and Bi (Bi; 99.99%, Alfa Aesar) for synthesizing $Mg_3Sb_{2-x}Bi_x$ (with

x=0, 0.2) were blended in mechanical milling and subsequently grounded in an agate mortar. The blended powders were then subjected to spark plasma sintering (SPS) at temperature 1073 K and a pressure of 50 MPa for holding time of 10 minutes yielding the pellets of 12.7 mm diameter and 2.5 mm thick. The SPS were performed in high vacuum and eliminates adsorptive gas and impurities existing on the surface of the powder particles which avoid the oxidation resulting to very clean samples. The SPS of powder materials involves simultaneous melting reaction and consolidation together resulting into a single phase materials. These single phase materials were crushed into powders and subsequently subjected to high energy mechanical ball milling (HEBM, Fritsch, Pulverisette-4) for periods of 10, 20 and 30 hours to achieve the nanostructured materials of polycrystalline Zintl phase. The ball-to-powder weight ratio was optimized at 25:1 and the whole process of milling was carried out in argon atmosphere with a speed of 400 rpm. In order to prevent re-welding and to promote fracturing of powder particles, 2 wt.% of stearic acid was added as a process control agent. The processing of the ball milled alloy powders was carried out in glove box (Mbraun, MB20) to avoid oxidation and other atmospheric contamination. The mechanically milled nanopowder were then consolidated by using again SPS at 873K and a pressure of 50 MPa for holding time of 3 minutes to maintain their nanostructured features. The SPS results a 12.7 mm diameter and 2.0 mm thick samples of nanostructured Zintl phase compounds. The volume densities of all the samples were measured using an Archimedes' kit. The density of the plasma sintered samples was observed to be 99% of the theoretical density.

2.2. Structural characterization

The gross structural characterization of bulk $Mg_3Sb_{2-x}Bi_x$ (x = 0 & 0.2) with their bulk nanostructured counterparts were carried out by powder X-ray diffractometer (Rigaku Mini Flex

II) using a graphite monochromator and CuKα radiation with wavelength λ ≈1.5406 Å along with $CuK\alpha_2$ filter and rotating anode equipped with powder 2θ diffractometer ranging from 20 to 80 degrees. The microstructure and compositional analysis were investigated by field emission scanning electron microscope (FE-SEM; Model: SUPRA40 VP, operating at 30 kV) equipped with energy dispersive spectroscopy (EDS) and transmission electron microscopy (TEM, Technai G^2T^{30}; W-Twin) operating at 300 KV. The TEM specimens were prepared in three steps and described elsewhere.[11-13]

2.3 Thermal and Electronic Transport Properties

The polished SPSed pellets of $Mg_3Sb_{2-x}Bi_x$ (with x=0 & 0.2) samples were used directly for thermal diffusivity measurements parallel to the pressing direction by using a laser flash system (Lineseis, LFA 1000) on disk-shaped thin specimens with approximate thickness of 1.5 mm and diameter of 12.7 mm. The disc specimens used for thermal diffusivity were sprayed with a layer of graphite in order to minimize errors due to emissivity. Specific heat was determined by a DSC instrument (822e Mettler Toledo). The thermal conductivity of all the samples was calculated using the relation, $\kappa = d \times Cp \times \rho$ wher κ is the thermal conductivity, d the thermal diffusivity, ρ the geometrical pellet density and Cp the specific heat capacity. The polished bars of about 3 × 1.5 × 10 mm were cut from the consolidated disks and are used to measure the electrical conductivity and Seebeck coefficient in a direction perpendicular to the pressing direction by employing commercial equipment (ULVAC, ZEM3) over the temperature range of 300 K to 773 K.

3. RESULTS AND DISCUSSION

3.1 X- ray Diffraction Analysis:

The phase purity of all the samples was verified prior to performing any transport properties measurement. The X-ray diffraction (XRD) pattern performed on the SPSed samples of $Mg_3Sb_{2-x}Bi_x$ (with x=0 & 0.2) are shown in Fig. 2(a). All the reflections can be indexed to β-Mg_3Sb_2 (JCPDS-00-003-0375) and no secondary phase was observed (Fig. 2a). Interestingly, XRD of both bulk nanostructured samples show the presence of peak broadening indicating the materials to be nanostructured. The average crystallite size calculated using Williamson-Hall method[48] is ~12 nm and 10 nm for nanostructured Mg_3Sb_2 and $Mg_3Sb_{1.8}Bi_{0.2}$ respectively after 30 hrs of ball-milling. The cell constants of both bulk and nanostructured samples were estimated by the POLSQ FORTRAN program[49] and are presented in supplementary table ST1. The XRD pattern of the bulk $Mg_3Sb_{2-x}Bi_x$ (x = 0 & 0.2) and nanostructured samples obtained by different periods of ball milling are shown in the supplementary figure S1.

3.2 Scanning Electron Microscopy:

For further confirming the phase and homogeneities at microscopic level, field emission-scanning electron microscopy (FE-SEM) investigation was carried out for bulk $Mg_3Sb_{2-x}Bi_x$ (x = 0 & 0.2) and their nanostructured counterparts. The homogeneities of all the samples were assessed by averaging the compositions at 4 different regions of each sample obtained by energy dispersive X-ray analysis (EADX). The average value of composition is shown in figure 2 marked as EDAX compositions indicating a homogeneous phase. The morphological evidence as presented in Fig 2 (a-d), for bulk Mg_3Sb_2, bulk $Mg_3Sb_{1.8}Bi_{0.2}$ and their bulk nanostructured counterparts respectively present almost similar contrasts of grains. The grain size of nanostructured samples is observed to be smaller as compared to their bulk counterparts. The FE-SEM EDAX mapping was recorded for all samples showing distribution of elemental phase in proper proportions to their stoichiometric compositions (Fig 2). The SEM-EADX spectrum of

bulk $Mg_3Sb_{2-x}Bi_x$ (x = 0 & 0.2) with their nanostructured counterparts were also recorded from a region marked by rectangle and their compositions are computed which are also presented as EDAX weight histograms (Fig. 2 c-d).

3.3 Transmission Electron Microscopy Investigation:

Figure 3 presents the transmission electron microscopy (TEM) of the nanostructured Mg_3Sb_2 and $Mg_3Sb_{1.8}Bi_{0.2}$ alloys. The microstructure features at lattice resolution was performed using high resolution transmission electron microscopy (HRTEM). In general, the HRTEM of these bulk nanostructured alloys reveals the nanoscale features and shows uniform microstructure with nanoscale crystallites, including some microstructural defects (Fig.3 b & e) which could be due to long hours of ball-milling.[23,24,43] The bright field electron micrograph obtained from the specimen of bulk nanostructured Mg_3Sb_2 exhibits a polycrystalline structure throughout the volume of the material (Fig. 3a). The micrograph shows grains with different sizes ranging from 4 nm to 40 nm. The number of crystallities and their size distribution is shown in the inset of figure 3a. Several lattice resolution images were recorded to understand the presence of different orientations of the crystallographic planes and their interface boundaries. Figure 3b presents HRTEM image obtained from sample showing several grains orientated along different planes of Mg_3Sb_2 and several joint interface boundaries. The micrograph (Fig. 3b) clearly reveals that the individual grains are truly crystalline with stacking of different planes and with random orientation with respect to each other. Several planes $11\bar{2}0$ (0.229 nm), $21\bar{3}3$ (0.127 nm) and $10\bar{1}0$ (0.398 nm) of Mg_3Sb_2 hexagonal crystal structure, are clearly seen in Fig. 3b. The elemental composition of Mg_3Sb_2 sample estimated from energy dispersive spectroscopy analysis (EDAX) attached with TEM (Fig 3c) reveals the composition very close to the nominal composition of Mg_3Sb_2 alloy. A bright field electron micrograph (Fig.3d) corresponding to the

specimen of bulk nanostructured $Mg_3Sb_{1.8}Bi_{0.2}$ shows a polycrystalline structure similar to Mg_3Sb_2 with relatively smaller grain sizes ranging from 3 nm to 30 nm. The crystallities size distribution is shown in the inset of figure 3d. The lattice scale images reveals the randomly distributed grains oriented in different planes $20\bar{2}4$ (0.134 nm), $10\bar{1}2$ (0.27 nm), $10\bar{1}3$ (0.206 nm) of Mg_3Sb_2 hexagonal crystal structure (Fig. 3e). Interestingly, the lattices associated with grains of bulk nanostructured $Mg_3Sb_{1.8}Bi_{0.2}$ are observed to be little distorted together with some misfit-type of dislocations at the interfaces as marked by arrows in Fig 3(e). The distortions in the lattices at microscopic level may be originated due to local strain due to substitution of heavy metal Bi at Sb site in the structure of Mg_3Sb_2. The elemental composition of $Mg_3Sb_{1.8}Bi_{0.2}$ sample estimated from energy dispersive spectroscopy analysis (EDAX) attached with TEM (Fig 3f) reveals the composition very close to the nominal composition of $Mg_3Sb_{1.8}Bi_{0.2}$ alloy.

3.4 Electronic transport properties

Fig. 4 shows the temperature dependence of the electronic transport properties of bulk $Mg_3Sb_{2-x}Bi_x$ (x = 0 & 0.2) and their nanostructured counterparts. The temperature dependent behavior σ (T) of all the samples presented in Fig 4 (a) reveals semiconducting behavior as it increases monotonically with rising temperature. Interestingly, the σ (T) of the nanostructured materials is noted to be lower than that of their normal bulk counterparts, not only at room temperature but over the entire temperature range. Fig. 4 (b) presents the temperature dependence behavior of Seebeck coefficient of all the samples. The Seebeck coefficients of the nanostructured samples are also observed to be higher than the normal bulk counterpart, over the entire temperature range as shown in Fig. 4(b). However, with increasing temperature beyond 673 K, the Seeback coefficient decreases slightly in all the samples. This decrease in Seeback coefficient at high temperature beyond 673 K is attributed due to thermally excited minority charge carriers

(electrons) similar to the case of several semiconducting materials.[16,50,51] The temperature dependence behavior of power factor of bulk $Mg_3Sb_{2-x}Bi_x$ (x = 0 & 0.2) and their nanostructured counterparts is plotted in Fig 4(c). The power factor of nanostructured samples is slightly decreased as compared to their bulk counterparts due to decrease in the electrical conductivity over the entire temperature range. The decrease in the power factors of nanostructured Mg_3Sb_2 and $Mg_3Sb_{1.8}Bi_{0.2}$ was noted to be a reduction of about 1.5% and 8.5% respectively in comparison to that of their bulk counterparts.

We have also performed the Hall Coefficient of all the samples at 300K. These data yield a carrier concentration of $1.1 \times 10^{20}/cm^3$ and $2.9 \times 10^{20}/cm^3$ for bulk Mg_3Sb_2 and $Mg_3Sb_{1.8}Bi_{0.2}$ respectively while a carrier concentration of $7.8 \times 10^{19}/cm^3$ and $9.2 \times 10^{19}/cm^3$ for nanostructured Mg_3Sb_2 and $Mg_3Sb_{1.8}Bi_{0.2}$ respectively was noted. Evidently, both the nanostructured materials exhibit lower carrier concentration as compared to their respective bulk counterparts.

The observed increase in Seeback coefficient and decrease in the electrical conductivity of both the nanostructured samples at room temperature compared to that for their respective bulk counterparts are consistent with their lower carrier densities as revealed by Hall measurements. The reduction in the carrier density of the nanostructured materials may be obtained either due to trapping of carriers at the interface barrier generated between the nano domains boundaries[23, 24] or it could be due to the defects which may be negatively charged and hence may trap the holes of the system, and thereby may decrease the carrier densities of the system.[52,53]Unfortunately, the trends S (T) and σ (T) displayed for the nanostructured materials are rather unusual and needs a detail high temperature Hall effect over the entire temperature range to understand the exact mechanism of electronic transport in these nanostructured materials.

3.5 Thermal transport properties

In addition to electronic transport, a thermal conductivity measurement is also equally important for quantifying the thermoelectric figure of merit (ZT). Figure 5 shows the temperature dependence of total thermal conductivity κ (T) of bulk $Mg_3Sb_{2-x}Bi_x$ (x = 0 & 0.2) and their nanostructured counterparts. The temperature dependent of κ decreases with temperature displaying T^{-1} type behavior which is commonly occurred in the bulk crystalline solids. The κ (T) of bulk $Mg_3Sb_{2-x}Bi_x$ (x = 0 & 0.2) and their nanostructured counterparts (Fig. 5a) decreases gradually with rising temperature. The reduction of the κ in nanostructured samples compared with their bulk counterparts is mainly due to the increased scattering of phonon by high density of grains boundaries in the sintered bulk nanostructured samples. It is worth mentioning that the high density of grains boundaries due to small crystallites developed employing high energy ball milling remains maintained in the bulk nanostructured samples obtained by using the spark plasma assisted reaction sintering (SPS) technique for consolidation.[24,43] To get a quantitative view of the effect of ball milling followed by SPS on phonon transport, the lattice thermal conductivity (κ_l) was estimated by subtracting the electronic contribution (κ_e) from the total thermal conductivity (κ). The electronic thermal conductivity (κ_e) can be estimated using the Wiedemann-Franz law (i.e. $\kappa_e = L \sigma T$, where L is Lorenz number, σ, the electrical conductivity and T, the temperature in K) which is presented in Fig 5(b). Here, we use the temperature dependent Lorenz number[54] and the bipolar contribution was taken into account by assuming $\kappa_{lattice} \sim T^{-1}$.[55] Figure 5(c) represents the temperature dependent lattice part of thermal conductivity. Within expectation, the lattice part of the thermal conductivity (Figure 5c) of both the nanostructured materials was decreased. For instance, we obtained $k_l \approx 1.38$ $Wm^{-1}K^{-1}$ and ~ 0.94 $Wm^{-1}K^{-1}$ at room temperature for the bulk Mg_3Sb_2 and nanostructured Mg_3Sb_2 respectively

while lattice thermal conductivity of ~1.18 $Wm^{-1}K^{-1}$ and ~0.90 $Wm^{-1}K^{-1}$ at room temperature were observed for bulk $Mg_3Sb_{1.8}Bi_{0.2}$ and nanostructured $Mg_3Sb_{1.8}Bi_{0.2}$ samples respectively. The lattice thermal conductivity (κ_l) of nanostructured Mg_3Sb_2 and $Mg_3Sb_{1.8}Bi_{0.2}$ samples at room temperature is observed to be about ~31% and ~ 24% lower than that of their respective bulk counterpart. The decrease in the lattice thermal conductivity is mainly attributed to a stronger boundary scattering in the nanostructured samples. There is no significant difference in total and lattice thermal conductivity (Fig. 5a & 5c). It appears that the lattice part is a large portion of the total thermal conductivity because the electronic part of thermal conductivity is negligibly small due to a very low value of electrical conductivity.

The most widely used model to understand the effect of grain size on the κ in ploycrystalline materials involves the relaxation time approaches of phonon boundary scattering mechanism described in the Callaway model.[56] However, the decrease of the thermal conductivity due to grain size effects in polycrystalline materials can also be understood by a simple model proposed by Nan and Birringer et al. [44,45] This simple model stands on the concept of the concept of Kapitza resistance which express the thermal boundary resistance present either at the interfaces of two materials or grains of the same material, with the macroscopic effective medium approaches (EMA).[57,58] The model describes the observed grain-size dependent κ of polycrystalline materials and, most importantly, offers a simple and practical method to determine the Kapitza resistance, thereby describing the grain-size effect on a quantitative basis. Although the shape and orientations of the crystallites may be fitted into the model, however, we consider the simplest case of a polycrystalline material assuming spherical grains with diameter d. Using this approximation, the thermal conductivity κ is given by

$$\frac{1}{\kappa} = \frac{1}{\kappa_0} + \frac{2R_k}{d} \quad \text{.....(1)}$$

where κ_0 is the bulk thermal conductivity of the grains and R_K is the Kapitza resistance of the grain boundaries. Equation 1 is used to determine both κ_0 and R_K by fitting the experimental data of κ^{-1} against d^{-1} at each temperature, assuming a linear approximation for all the nanostructured samples. Figure 6(a & b) presents the experimental data and fitted lines in the range 373-773 K for Mg_3Sb_2 and $Mg_3Sb_{1.8}Bi_{0.2}$ respectively. The fitted values of κ_0 and R_K are taken from Table 1 and plotted as a function of temperature in Figure 7. From these values, κ_0 and R_K at 323 K (RT) were also extrapolated and are shown in Table 1. In Table 1, the value of R_K at 323 K is taken to be the same as those at 373 and 423 K, since the decrease in R_K with decreasing temperature has already reached its limit in this range, as shown in Figure 7. This is in agreement with previous studies of other semiconductor systems,[45,59-61] where R_K was found to be almost independent of temperature over a wide range around room temperature. For example, both n- and p-$Si_{0.8}Ge_{0.2}$ alloys were reported to have approximately the same value of R_K=5.0 x 10^{-8} m^2KW^{-1} in studies where the effect of the grain size on the transport properties is discussed.[62] Nan and Birriger[44,45] have also introduced the concept of Kapitza length, $L_K = R_K\kappa_0$, as an important characteristic length to quantify the grain-size dependence of κ for a given material. The values of L_K for the $Mg_3Sb_{2-x}Bi_x$ (x = 0 & 0.2) alloys have therefore been calculated and given in Table 1. According to Equation 1, k decreases to $K_0/2$ when d = 2 L_K, and d = 0.5 L_K is required to further reduce κ at 20% of κ_0. At room temperature, L_K equals 55 and 43 nm for Mg_3Sb_2 and $Mg_3Sb_{1.8}Bi_{0.2}$ samples respectively which is smaller as compared to the typical values of L_K in the range 250-800 nm for Si-Ge alloys.[45,62] One may easily anticipate that κ of these samples is very low which may cause the boost in the thermoelectric figure-of-merit (ZT).

3.6 Thermoelectric figure of merit (ZT)

The temperature dependence of ZT for bulk $Mg_3Sb_{2-x}Bi_x$ (x = 0 & 0.2) and their nanostructured counterparts are calculated which is displayed in Fig 8. The ZT of all the samples are observed increasing with increasing temperature. The maximum ZT ≈ 0.94 at 773 K for bulk nanostructured $Mg_3Sb_{1.8}Bi_{0.2}$ was optimized, which is significantly enhanced by > 55 % when compared with its bulk counterpart (ZT ~0.6 for $Mg_3Sb_{1.8}Bi_{0.2}$) and about > 250 % enhanced in ZT is estimated when compared with parent bulk Mg_3Sb_2 alloy (ZT ≈ 0.26 for Mg_3Sb_2). The enhancement in ZT is primarily due to drastic reduction in thermal conductivity and with simultaneous increase in the Seebeck coefficient.

3.7 Thermoelectric Compatibility Factor:

The thermoelectric compatibility factor (s) is also an important parameter which plays a vital role in the formation of thermoelectric device. This new physical parameter was suggested by Synder el. at.[63] in 2003. The value of thermoelectric compatibility factor of any material is described its applicability to be used as a segmented couples with other material for the fabrication of the thermoelectric device in power generation. The thermoelectric compatibility factor (s) is the function of temperature and it depends upon the Seebeck coefficient (α), given as

$$S = \frac{\sqrt{1+ZT}-1}{\alpha T} \quad \text{.....(2)}$$

where α is Seebeck coefficient in volts and T is temperature in Kelvin.

Now the evaluation of S in thermoelectric materials is needed to find out the possibility of the counterpart of the TE device and is also required to achieve maximum thermoelectric efficiency.

It is well know that the two different materials may be used in the segmented thermoelectric generator, if their thermoelectric compatibility factors are same or less than a factor of 2.[64-66]

The compatibility factors of bulk and nanostructured samples of $Mg_3Sb_{2-x}Bi_x$ (with x=0, 0.2) are computed and presented in Fig 9. Interestingly, the compatibility factors of both nanostructured samples are large enough at high temperature when compared to that of their respective bulk counterparts. The compatibility factor of nanostructured $Mg_3Sb_{1.8}Bi_{0.2}$ alloy was maximized to be ~ +1.5 V^{-1} at 773K. We have also compared the compatibility factors of present study with the compatibility factors of several state-of-the-art p-type thermoelectric materials with high ZT and the same is displayed in Fig 9(b). Interestingly, the compatibility factor of bulk nanostructured $Mg_3Sb_{1.8}Bi_{0.2}$ alloy of present study is observed to be comparable to that of the other state-of-the-art p-type thermoelectric materials with high ZT as shown in figure 9 (b).[67] Hence, bulk nanostructured $Mg_3Sb_{1.8}Bi_{0.2}$ is a suitable p-type material for segmentation with broad range of other state-of-the art TE materials (within about a factor of 2) to gain highest efficiency benefit for the thermoelectric devices used in power generation. Thus, owing to the dual advantages of reasonably high ZT and high value of compatibility factor of present bulk nanostructured $Mg_3Sb_{1.8}Bi_{0.2}$ materials, they evolve as potentially good materials for the replacement to the segmentation with the other state-of-the-art p-type thermoelectric materials for the use of thermoelectric device fabrication.

4. Conclusions and Future Prospects:

Nanostructuring of $Mg_3Sb_{2-x}Bi_x$ (x = 0 & 0.2) employing high energy mechanical milling followed by spark plasma sintering (SPS) results a significant increase in overall thermoelectric figure of merit (ZT) in comparison with that of their respective normal bulk counterparts. A peak

ZT ≈ 0.94 at 773 K for bulk nanostructured $Mg_3Sb_{1.8}Bi_{0.2}$ alloy was optimized, which is about 55 % higher when compared with its bulk counterpart (ZT ~0.6 for $Mg_3Sb_{1.8}Bi_{0.2}$) and about > 250 % larger in comparison to the parent bulk Mg_3Sb_2 alloy (ZT ≈ 0.26 for Mg_3Sb_2). The enhancement in ZT is primarily due to drastic reduction in thermal conductivity. Analysis of thermal conductivity data in the light of macroscopic model proposed by Nan et al reveals that the effect of grain boundary scattering on κ relates to the largest part of its cause and is genuine. Additionally, this model also suggests that a further significant reduction of κ would occur if these bulk nanostructured samples could be prepared with sizes comparable to or even much smaller than the estimated Kapitza length of 54 nm at 323 K in the present investigation. It may be inferred here that the effect of nanostructuring on the reduction of thermal conductivity would be even more significant in those nanostructured materials which exhibit larger Kapitza resistances than these materials. Combined with the reasonably high ZT and high value of compatibility factor of present bulk nanostructured $Mg_3Sb_{1.8}Bi_{0.2}$ materials, with its cheap, abundant, and non-toxic constituent elements (i.e. Mg, Sb, and Bi) evolve as a potentially good materials for the utilization of the segmentation with other state-of-the-art p-type thermoelectric materials when deployed to the process of thermoelectric device fabrication. We strongly believe that the present nanostructuring approach can be extended to other Zintl phase compounds for improving the thermoelectric properties which has been seldom seen for this particular family of compounds.

Acknowledgement:

This work was financially supported by CSIR-TAPSUN (CSIR-NWP-54) programme. The authors are graceful to the Ex-Director, Prof. R. C. Budhani (Ex-Director, CSIR-NPL), for his constant mentoring and support for this project. The authors thank Dr. Jiji Pullikotil and Dr. T.D. Senguttuvan (CSIR-

NPL) for useful discussions and comments. One of the authors AB greatly acknowledges UGC-CSIR for financial support. The technical support rendered by Mr Radhey Shyam and Mr Naval Kishor Upadhyay is gratefully acknowledged.

References:

1. B. Raton, *CRC Handbook of Thermoelectrics,* CRC, Florida, USA, 1995.
2. G. S. Nolas, J. Sharp, and H. Goldsmid, *Thermoelectrics: Basic Principles and New Materials Developments,* Springer, New York, 2001.
3. T. M. Tritt and M. A. Subramanian, *MRS Bull.*, 2006, **31**, 188.
4. L.E. Bell, *Science,* 2008, **321**, 1457–1461.
5. G. J. Snyder and E. S. Toberer, *Nat. Mater.*, 2008, **7**, 105**.**
6. J. Yang, H.-L. Yip, A. K.-Y. Jen, *Adv. Energy Mater.* 2013, **3**, 549.
7. S. N. Girard, J. He, X. Zhou, D. Shoemaker, C. M. Jaworski, C. Uher, V. P. Dravid, J. P. Heremans, M. G. Kanatzidis, *J. Am. Chem. Soc.* 2011, **133**, 16588.
8. H. Wang, Y. Pei, A. D. LaLonde, G. J. Snyder, *Adv. Mater.* 2011, **23**, 1366.
9. S. N. Guin, A. Chatterjee, D. S. Negi, R. Datta and K. Biswas, *Energy Environ. Sci.*, 2013, **6**, 2603.
10. X. Liu, H. Wang, L. Hu, H. Xie, G. Jiang, G. J. Snyder, X. Zhao, T. Zhu, *Adv. Energy Mater.* **2013**, *3*, 1238.
11. A. Bhardwaj, A. Rajput, A. K. Shukla, J. J. Pulikkotil, A. K. Srivastava, A. Dhar, G. Gupta, S. Auluck, D. K. Misra, R. C. Budhani, *RSC Adv.* 2013, **3**, 8504.
12. A. Bhardwaj and D. K. Misra, *RSC Adv.*, 2014, **4**, 34552.
13. A. Bhardwaj, A. K. Shukla, S. R. Dhakate, D. K. Misra, *RSC Adv.,* 2015*,* **5**, 11058.
14. A. Banik, U. S. Shenoy, S. Anand, U. V. Waghmare, and K. Biswas, *Chem. Mater.*, 2015, **27**, 581.
15. D. K. Misra, A. Bhardwaj, S. Singh, *J. Mater. Chem.*, 2014, **2**, 11913- 11921
16. D. K. Misra, A. Rajput, A. Bhardwaj, N. S. Chauhan and S. Singh *App. Phy. Lett.,* 2015, **106**, 103901.
17. S. N. Guin, J. Pan, A. Bhowmik, D. Sanyal, U. V. Waghmare, and K. Biswas, *J. Am. Chem. Soc.*, 2014, **136**, 12712.
18. Y. Pei, H. Wang and G. J. Snyder, *Adv. Mater.*, 2012, **24**, 6124.

19. K. F. Hsu, S. Loo, F. Guo, W. Chen, J. S. Dyck, C. Uher, T. Hogan, E. K. Polychroniadis and M. G. Kanatzidis, *Science*, 2004, **303**, 818.
20. J. Androulakis, K. F. Hsu, R. Pcionek, H. Kong, C. Uher, J. J. D'Angelo, A. Downey, T. Hogan and M. G. Kanatzidis, *Adv. Mater.*, 2006, **18**, 1170.
21. J.-F. Li, W.-S. Liu, L.-D. Zhao, M. Zhou, *NPG Asia Mater.* 2010, **2**, 152.
22. S. N. Guin, D. S. Negi, R. Datta and K. Biswas, *J. Mater. Chem. A*, 2014, **2**, 4324.
23. G. Joshi, H. Lee, Y. Lan, X. Wang, G. Zhu, D. Wang, R. W. Gould, D. C. Cuff, M. Y. Tang, M. S. Dresselhaus, G. Chen and Z. F. Ren, *Nano Lett.*, 2008, **8**, 4670.
24. A. Bhardwaj, D. K. Misra, J. J. Pulikkotil, S. Auluck, A. Dhar, R. C. Budhani, *Appl. Phys. Lett.,* 2012, **101**, 133103.
25. A. Bhardwaj and D. K. Misra, *J. Mater. Chem. A*, 2014, **2**, 20980.
26. S. K. Bux, J. P. Fleurial, R. B. Kaner, *Chem. Comm.*, 2010, **46**, 8311.
27. J. R. Szczech, J. M. Higgins, S. Jin, J. Mater. Chem. 2011, **21**, 4037.
28. M.S. Dresselhaus, G. Chen, M.Y. Tang, R.G. Yang, H. Lee, D.Z. Wang, Z. F. Ren, J. P. Fleurial and P. Gogna, *Adv. Mater.*, 2007, **19**, 1043.
29. K. Biswas, J. He, Q. Zhang, G. Wang, C. Uher, V. P. Dravid, M. G. Kanatzidis, *Nature Chemistry,* 2011, **3**, 160.
30. R. Venkatasubramanian, E. Siivola, T. Colpitts and B. O'Quinn, *Nature*, 2001, **413**, 597.
31. T. C. Harman, P. J. Taylor, M. P. Walsh and B. E. LaForge, *Science*, 2002, **297**, 2229.
32. A. I. Hochbaum, R. Chen, R. D. Delgado, W. Liang, E. C. Garnett, M. Najarian, A. Majumdar and P. Yang, *Nature*, 2008, **451**, 163.
33. A. I. Boukai, Y. Bunimovich, J. Tahir-Kheli, J.-K. Yu, W. A. Goddard Iii and J. R. Heath, *Nature*, 2008, **451**, 168.
34. A. J. Minnich, M. S. Dresselhaus, Z. F. Ren and G. Chen, *Energy Environ. Sci.*, 2009, **2**, 466.
35. G. G. Yadav, J. A. Susoreny, G. Zhang, H. Yang and Y. Wu, *Nanoscale*, 2011, **3**, 3555.
36. Z. -G. Chen, G. Han, L. Yang, L. Cheng, J. Zou, *Progress in Natural Science: Materials International*, 2012, **22**, 535.
37. H. Bredt, L. F. Kendall, *Proceedings—IEEE/AIAA* 1966.
38. D. M. Verbrugge, J. B.J. Van Zytveld, *Non-Cryst. Solids* 1993, **736**, 156.

39. T. Kajikawa, N. Kimura, T.Yokoyama, *Proceedings of the 22nd International Conference on Thermoelectrics*, 2003, 305.
40. C. L. Condron, S. M. Kauzlarich, F. Gascoin, G. J. Snyder, *J. of Sol. Stat. Chem.*, 2006, **179**, 2252.
41. D. J. Singh and D. Parker *J. of Appl. Phys*. 2013, **114**, 143703
42. S. Bathula, R. C. Anandani, A. Dhar, and A. K. Srivastava, *Mater. Sci. Eng. A,* 2012, **545**, 97.
43. S. Bathula, M. Jayasimhadri, N. Singh, A. K. Srivastava, J. J. Pulikkotil, A. Dhar, and R. C. Budhani, *App. Phy. Lett.* 2012, **101**, 213902.
44. C.-W. Nan, R. Birriger, D. R. Clarke, H. Gleiter, *J. Appl. Phys.* 1997, **81**, 6692.
45. C.-W. Nan, R. Birriger, *Phys. Rev B: Condens. Matter,* 1998, **57**, 8264.
46. P. L. Kapitza, *J. Phys.* 1941, **4**, 181.
47. E. T. Swartz, R. O. Pohl, *Rev. Mod. Phys.* 1989, **61**, 605.
48. B. D. Cullity and S. R. Stock, *Elements of X-Ray Diffraction, Vol. 167, 3rd ed.,* Prentice-Hall, Inc., 2001.
49. D. Keazler, D. Cahen, J. Lbers *POLSQ FORTRAN program*, IL: Northwestern University Evanston, **1984**.
50. J. L. Mi, X. B. Zhao, T. J. Zhu, J. P. Tu, *J Phys D: Appl Phys.*, 2008, **41**, 205403.
51. G. S. Nolas, J. Sharp, H. J. Goldsmid, *Thermoelectric*, Springer, Berlin, **2001**.
52. C. Bae, T. Böhnert, J. Gooth, S. Lim, S. Lee, H. Kim, S. Heimann, S. Schulz, H. Shin and K. Nielsch, *Semicond. Sci. Technol*. 2014, **29**, 064003.
53. P. Pichanusakorn, P. Bandaru, *Materials Science and Engineering R,* 2010, **67**, 19.
54. S. A. Chambers, T. Droubay, T. C. Kasper, M. J. Gutowski, *Vac. Sci. Technol. B,* 2004, **22**, 2205.
55. L. M. Watson, C. A. W. Marshall, C. P. Cardoso, *J. Phys. F: Met. Phys,* 1984, **14**, 113.
56. J. Callaway, *Phys. Rev.* 1959, **113**, 1046.
57. D. A. G. Bruggeman, *Ann. Phys. (Leipzig),* 1935, **24**, 636.
58. R. Landauer, *J. Appl. Phys.* 1952, **23**, 779.
59. R. J. Stoner, H. J. Maris, *Phys. Rev. B: Condens. Matter* 1993, **48**, 16373.

60. D. S. Smith, S. Fayette, S. Grandjean, C. Martin, R. Telle, T. Tonnessen, *J. Am. Ceram. Soc.*, 2003, **86**, 105.
61. M. S. Toprak, C. Stiewe, D. Platzek, S. Williams, L. Bertini, E. Müller, C. Gatti, Y. Zhang, M. Rowe, and M. Muhammed, *Adv. Fuct. Mater,* 2004, **14**, 1190.
62. D. M. Rowe, L. W. Fu, S. G. K. Williams, *J. Appl. Phys.* 1993, **73**, 4683.
63. G. J. Snyder and T. S. Ursell, *Phys. Rev. Lett.*, 2003, **91**, 148301.
64. G. J. Snyder, *Appl. Phys. Lett., 2004,* **84**, 2436.
65. E. Macia, *Phys. Rev. B,* 2004, **70**, 100201.
66. S. R. Brown, S. M. Kauzlarich, F. Gascoin, and G. J. Snyder, *Chem. Mater.* 2006, **18**, 1873.
67. P. H. Ngan, D. V. Christensen, G. J. Snyder, Le. T. Hung, S. Linderoth, N. Van Nong, and N. Pryds, *Phys. Status Solidi A,* 2014, **211**, 9.

Figure Caption:

Figure 1. X-ray diffraction (XRD) pattern of bulk $Mg_3Sb_{2-x}Bi_x$ (x = 0 & 0.2) with their bulk nanostructured counterparts.

Figure 2: FE-SEM micrographs of (a) bulk Mg3Sb2 parent compound showing polycrystalline nature of sample along with the elemental EDAX mapping and EADX spectrum of Mg3Sb2 confirming the composition, very close to Mg3Sb2 as shown in the bottom of the figure 2(a); (b) SEM image of Mg3Sb1.8Bi0.2 revealing almost similar type of morphology of Mg3Sb2 and the elemental EDAX mapping images shown demonstrates the presence of all three constituent elements (i.e. Mg, Sb & Bi) and the composition close to its nominal composition; and c-d) showing the SEM images along with the EADX spectrum and elemental quantifications of bulk nanostructured samples of Mg3Sb2 and Mg3Sb1.8Bi0.2 respectively.

Figure 3 a) TEM image obtained from the specimen of nanostructured Mg_3Sb_2 showing polycrystalline grains, inset shows the crystallite size distribution. b) the lattice scale image

of nanostructured Mg_3Sb_2 exhibiting the presence of different orientations of the crystallographic planes and their interface boundaries; c) EDAX-TEM patterns recorded from nanostructured Mg_3Sb_2 confirming its exact composition; d) Bright field electron micrograph recorded from the specimen of nanostructured $Mg_3Sb_{1.8}Bi_{0.2}$ showing polycrystalline grains, inset shows the crystallite distribution e) The HRTEM image of nanostructured $Mg_3Sb_{1.8}Bi_{0.2}$ demonstrating distorted lattices; f) EDAX-TEM patterns recorded from nanostructured $Mg_3Sb_{1.8}Bi_{0.2}$ confirming its exact composition.

Figure 4: Temperature dependence of a) the electrical conductivity, σ(T); b) the Seebeck coefficient, α(T); c) the power Factor, P.F. ($\sigma\alpha^2$ (T)) of bulk $Mg_3Sb_{2-x}Bi_x$ (x = 0 & 0.2) and their nanostructured counterparts.

Figure 5: Temperature dependence behavior of a) the total thermal conductivity, κ (T); b) the electronic thermal conductivity, κ_e(T); c) the lattice thermal conductivity, κ_L(T) of bulk $Mg_3Sb_{2-x}Bi_x$ (x = 0 & 0.2) and their nanostructured counterparts.

Figure 6: 1/κ versus 1/d plots for different grain sizes for different nanostructured materials obtained after milling of 10, 20 and 30 hrs. The points are experimental data while the lines are calculated according to the fit of Equation 1 to the experimental data.

Figure 7: Calculated thermal conductivity κ_0 and Kapitza resistance R_k versus temperature for both Mg_3Sb_2 and $Mg_3Sb_{1.8}Bi_{0.2}$ alloys.

Figure 8: Temperature dependence of thermoelectric figure of merit of bulk $Mg_3Sb_{2-x}Bi_x$ (x = 0 & 0.2) and their nanostructured counterparts.

Figure 9: The temperature dependent thermoelectric compatibility factor (s) for bulk p-type $Mg_3Sb_{2-x}Bi_x$ (x = 0 & 0.2) and their nanostructured counterpart (b) Comparison of the

compatibility factors of nanostructured $Mg_3Sb_{1.8}Bi_{0.2}$ alloy with the compatibility factor (s) for some state-of-the-art p-type thermoelectric materials with their high ZT.

Table 1**:** The fitted values of bulk thermal conductivity (κ_0) Kapitza resistance (R_k) and Kapitza length (L_k).

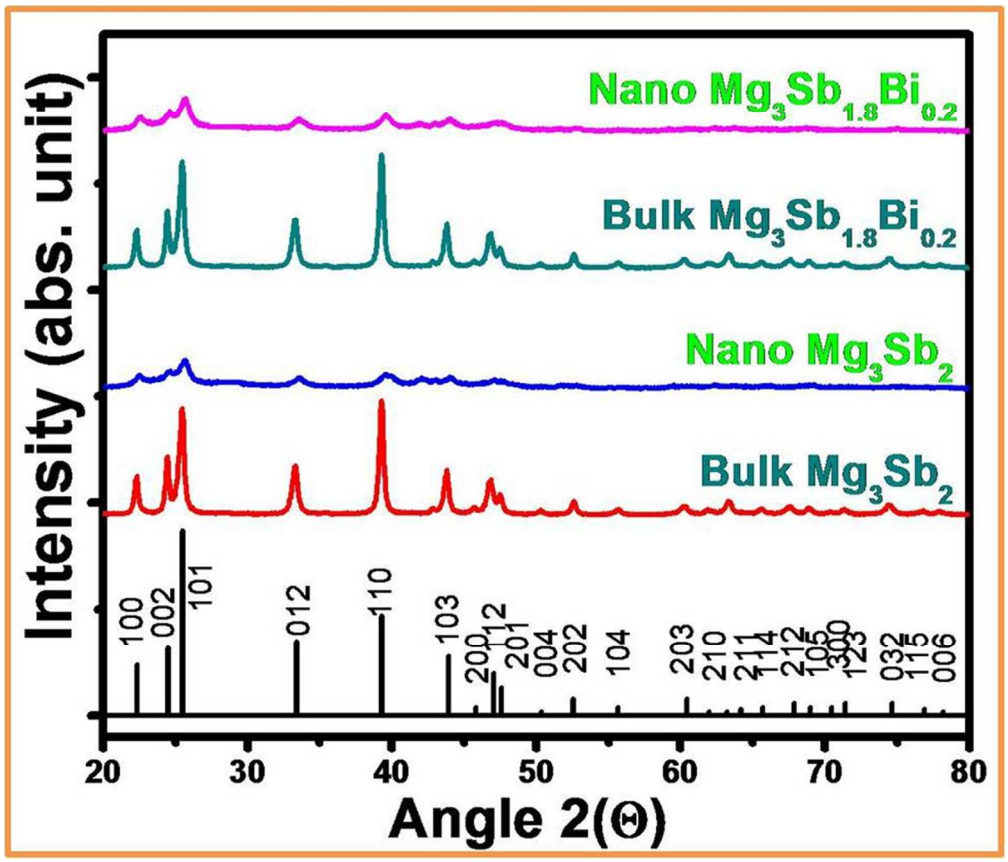

165x140mm (150 x 150 DPI)

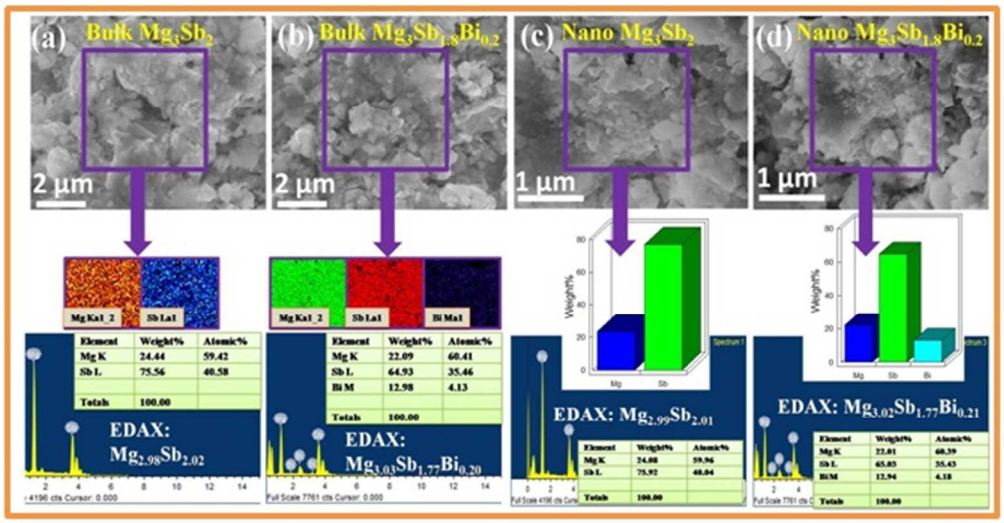

176x91mm (96 x 96 DPI)

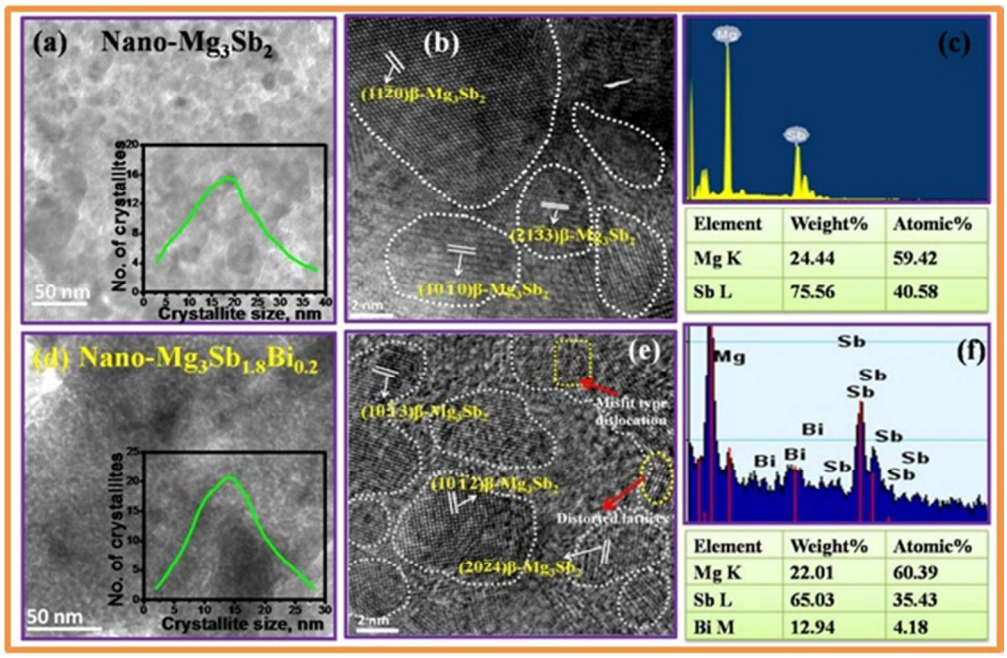

167x109mm (96 x 96 DPI)

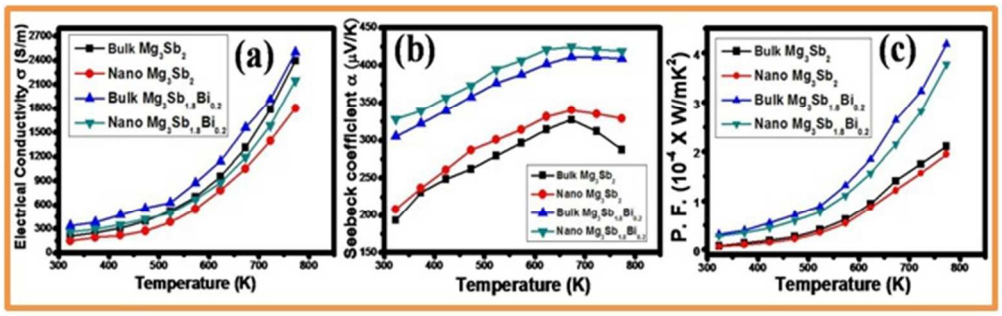

177x55mm (96 x 96 DPI)

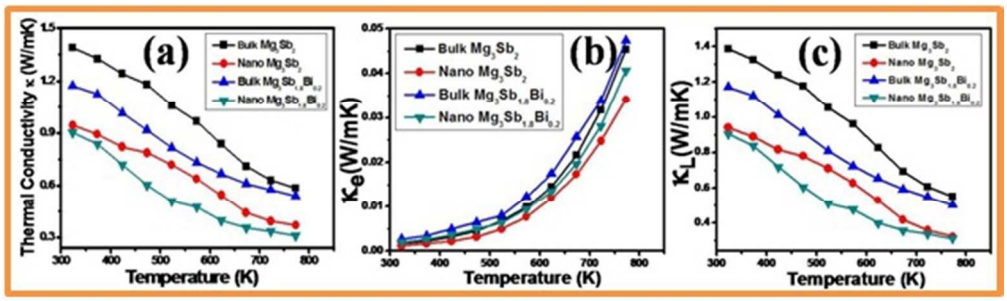

167x49mm (96 x 96 DPI)

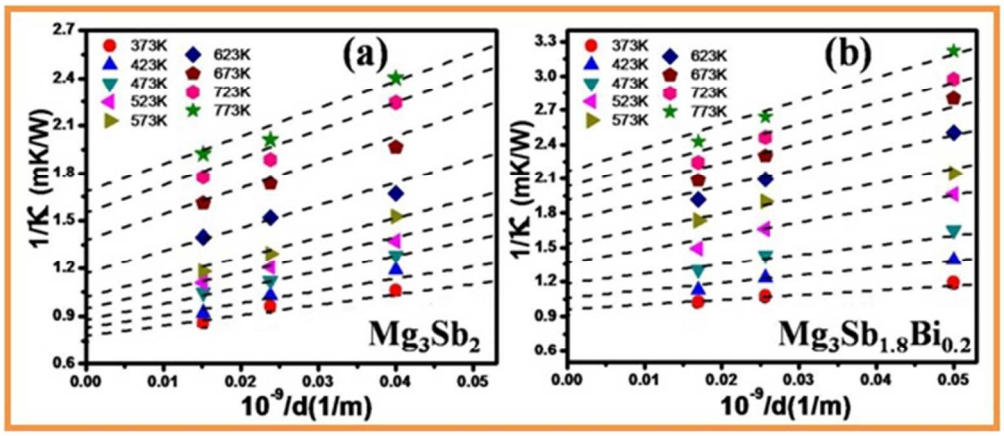

168x72mm (96 x 96 DPI)

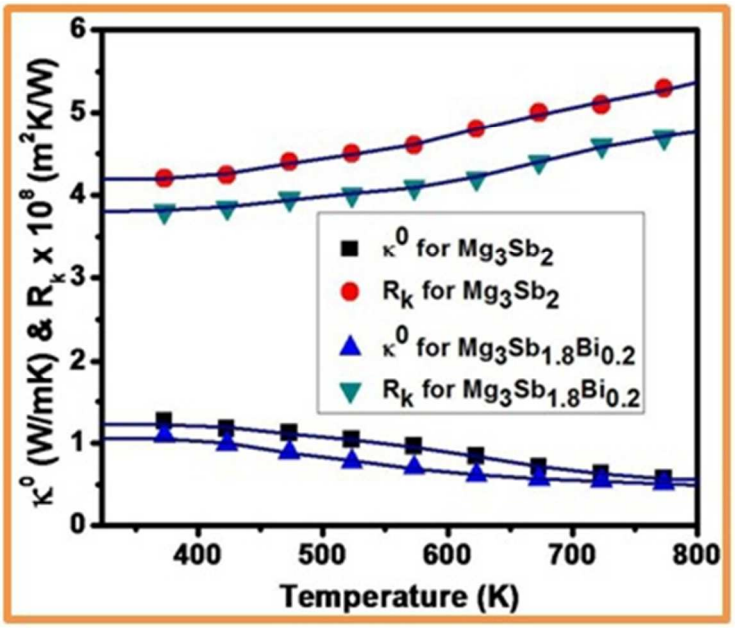

97x82mm (96 x 96 DPI)

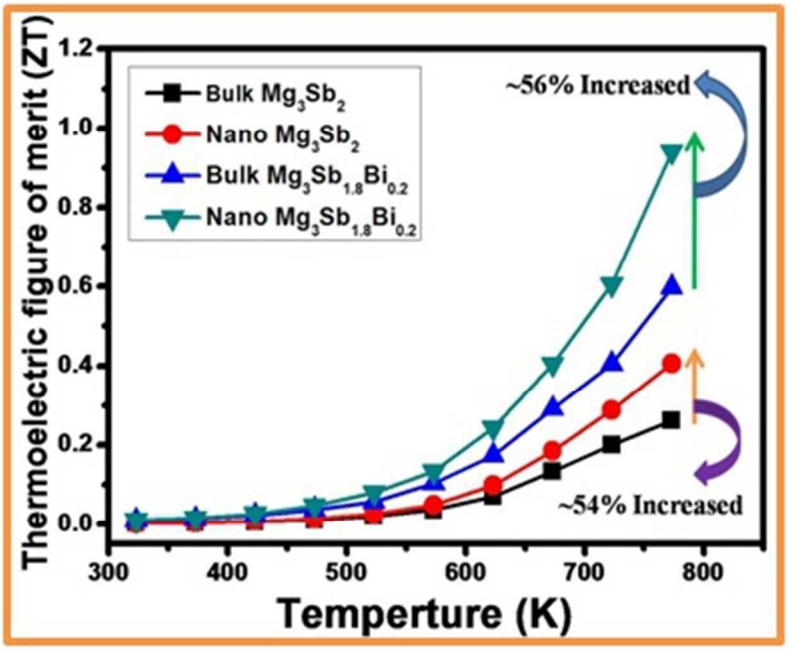

104x85mm (96 x 96 DPI)

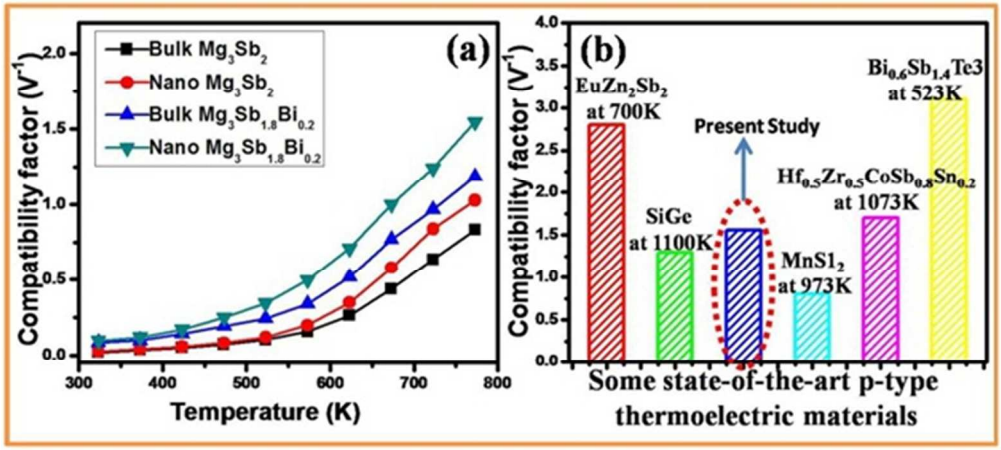

166x74mm (96 x 96 DPI)

Table 1. The fitted values of bulk thermal conductivity (κ_0) Kapitza resistance (R_k) and Kapitza length (L_k).

Mg_3Sb_2			
T (K)	**K^o ($Wm^{-1}K^{-1}$)**	**R_k x 10^{-8} (m^2KW^{-1})**	**L_k (nm)**
323	1.32	4.2	55.44
373	1.26	4.2	52.92
423	1.17	4.24	49.61
473	1.12	4.4	49.28
523	1.04	4.5	46.8
573	0.96	4.6	44.16
623	0.84	4.8	40.32
673	0.71	5	35.50
723	0.63	5.1	32.13
773	0.57	5.3	30.21
$Mg_3Sb_{1.8}Bi_{0.2}$			
T (K)	**κ^o ($Wm^{-1}K^{-1}$)**	**R_k x 10^{-8} (m^2KW^{-1})**	**L_k (nm)**
323	1.14	3.8	43.32
373	1.09	3.8	41.42
423	0.99	3.85	38.115
473	0.89	3.96	35.244
523	0.78	4	31.20
573	0.7	4.1	28.70
623	0.62	4.2	26.04
673	0.57	4.4	25.08
723	0.54	4.6	24.84
773	0.51	4.7	23.97